APL Photonics

Selective near-perfect absorbing mirror as a spatial frequency filter for optical image processing

Cite as: APL Photonics 4, 100801 (2019); https://doi.org/10.1063/1.5113650
Submitted: 06 June 2019 . Accepted: 12 September 2019 . Published Online: 01 October 2019

Lukas Wesemann, Evgeniy Panchenko, Kalpana Singh, Enrico Della Gaspera, Daniel E. Gómez, Timothy J. Davis, and Ann Roberts

Selective near-perfect absorbing mirror as a spatial frequency filter for optical image processing

Cite as: APL Photon. 4, 100801 (2019); doi: 10.1063/1.5113650
Submitted: 6 June 2019 • Accepted: 12 September 2019 •
Published Online: 1 October 2019

Lukas Wesemann,[1,a] Evgeniy Panchenko,[1] Kalpana Singh,[1] Enrico Della Gaspera,[2] Daniel E. Gómez,[2] Timothy J. Davis,[1] and Ann Roberts[1]

AFFILIATIONS

[1]School of Physics, The University of Melbourne, Melbourne, VIC 3010, Australia
[2]School of Science, RMIT University, Melbourne, VIC 3001, Australia

[a]Electronic mail: lwesemann@student.unimelb.edu.au

ABSTRACT

Spatial frequency filtering is a fundamental enabler of information processing methods in biological and technical imaging. Most filtering methods, however, require either bulky and expensive optical equipment or some degree of computational processing. Here, we experimentally demonstrate real-time, on-chip, all-optical spatial frequency filtering using a thin-film perfect absorber structure. We experimentally demonstrate edge enhancement of an amplitude image and conversion of phase gradients to intensity modulation in an image. The device is used to demonstrate enhancement of an image of pond algae.

I. INTRODUCTION

Spatial frequency filtering underpins many widely used imaging methods ranging from visualizing phase variations in transparent objects, such as live biological cells,[1] to approaches for image enhancements used for object and face recognition.[2] Most common optical methods for spatial frequency filtering, however, involve relatively bulky optical systems,[3,4] while other popular image processing techniques rely on computation.[2] While the use of conventional optical components places limits on the potential for miniaturization, the conversion from optical to electrical signals as well as computation time for electronic approaches places limits on applications requiring high throughput, rapid processing, and low energy consumption.[5–7] Nanophotonic, all-optical image processing methods, on the other hand, offer ultracompact, real time, and low power alternatives for use in emerging integrated analog optical computing and image processing devices.[8,9] Diffractive object plane filtering using a thick grating was demonstrated decades ago,[10] but with advances in nanofabrication techniques, there is emerging interest in using subwavelength thickness films and structures to perform nondiffractive optical image processing.[9,11–18] While nanophotonic devices usually require complex fabrication schemes, thin-film approaches have recently gained attention as solutions for all-optical image processing.[19–22] Experimental demonstrations of optical image processing using thin films have focused on optical computing spatial differentiation but have been confined to performing operations in one dimension[23] and are still relatively bulky.[24] While directional operations may be desirable in some cases, other applications might require processing in two dimensions. Inspired by the concept of the Salisbury screen[25] developed for radio frequencies, we here report a simple two layer thin-film, near-complete absorption device that performs all-optical two-dimensional spatial frequency filtering of an incoming wavefield, with the relevant thickness of the device being less than 200 nm. The performance of thin film absorbers is well known to be dependent on the angle of incidence of light, and this spatial frequency filtering capability of suggests an avenue for the development of ultracompact, all-optical information processing devices. Due to their relatively small footprint and simple fabrication process, thin film absorber devices have the potential to be part of next generation image processing components in handheld medical diagnostic and other portable sensing systems.[26] Here, we demonstrate experimentally the edge enhancement of an amplitude

image and conversion of phase gradients into intensity modulation using a thin-film absorber.

II. SPATIAL FREQUENCY FILTERING CAPABILITY OF THIN FILM ABSORBERS

A Salisbury screen consists of a thin, absorbing, but semitransparent layer of metal separated from a reflective substrate by a dielectric spacer layer. For a dielectric layer with a thickness of approximately a quarter wavelength, multiple reflections lead to "perfect" absorption at a specific wavelength. The condition for absorption is, however, also sensitive to the angle of incidence θ, so that the reflectance depends on the transverse component $k_x = k \sin\theta$ of the spatial frequency of an incident plane wave with wave number k. Since an arbitrary incident wavefield can be decomposed into a spectrum of plane waves propagating in different directions with different spatial frequencies, the dependence of absorption on the angle of incidence provides a mechanism to filter low spatial frequencies from the reflected field. As an example, consider a device consisting of a gold film with thickness $d_1 = 31$ nm and a silicon dioxide spacer layer of thickness $d_2 = 155$ nm on a thick gold substrate, as illustrated in Fig. 1(a). Here, we consider SiO_2 as the material for the spacer layer, but other dielectrics would yield similar results with slightly increased (for lower refractive index) or decreased (for higher refractive index) angular sensitivity. Thicknesses were chosen to minimize reflectance at normal incidence at a wavelength of $\lambda = 631$ nm, although grazing angles are strongly reflected. The optical properties of bulk gold[27] and fused silica[28] were taken from the literature. The reflectance spectrum from the device as a function of angle of incidence is shown for both p- and s-polarized light in Figs. 1(b) and 1(c), respectively. Negligible reflection can be seen at normal incidence, but the reflectance increases with angle of incidence [cf. Fig. 1(d)]. This structure, therefore, suppresses plane waves with low spatial frequencies while reflecting high spatial frequencies at the design wavelength, demonstrating the capacity for spatial frequency filtering. This property holds for both p- and s-polarizations with only small differences between the two in sensitivity of the reflectance to k_x.

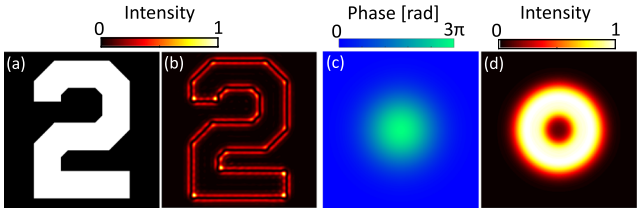

FIG. 2. Numerical demonstration of all optical image processing by the thin film absorber structure at $\lambda = 631$ nm using unpolarized light. Edge enhancement in an amplitude image with (a) the original and (b) the intensity of the reflected image. Visualization of a phase-only gradient with (c) the Gaussian phase modulation and (d) the intensity of the reflected image. Intensities are normalized to the brightest pixel. Spatial frequencies corresponding to evanescent fields, i.e., $k_x^2 + k_y^2 > k_0^2$, are neglected. The image is 15 × 15 μm^2 in size.

Figure 2 shows the results of numerical simulations of image processing by reflection from a Salisbury screen of both an amplitude and a pure phase object. In the case of plane wave illumination of the object of interest, the resulting transmitted wavefield incident on the screen can be decomposed into plane wave p- and s-polarization components with $\tilde{E}_{0p}(k_x, k_y)$ and $\tilde{E}_{0s}(k_x, k_y)$ denoting their Fourier transforms, respectively. The amplitude reflectances for p- and s-polarization are given by $r_p(k_x, k_y)$ and $r_s(k_x, k_y)$, and these play the role of optical transfer functions. The p- and s-components of the angular spectrum of the reflected wavefield are, therefore, given by

$$\tilde{E}_{\mathrm{ref},p}(k_x, k_y) = r_p \tilde{E}_{0p}(k_x, k_y), \tag{1a}$$

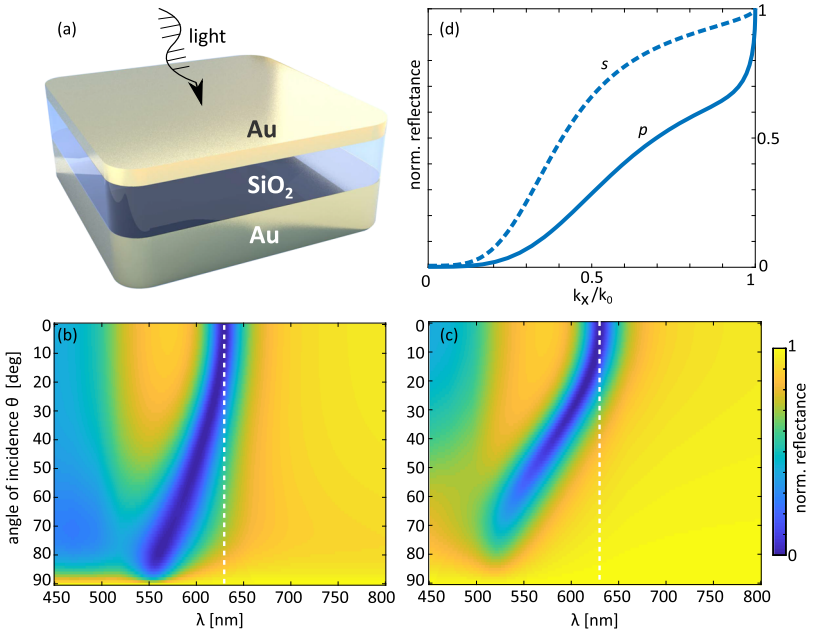

FIG. 1. Salisbury screen as a highpass spatial frequency filter. (a) Thin film configuration, (b) and (c) calculated reflectance spectrum as a function of angle of incidence for p- and s-polarization, and (d) calculated reflectance for p- (solid line) and s-polarization (dashed line) evaluated at the absorption wavelength $\lambda = 631$ nm.

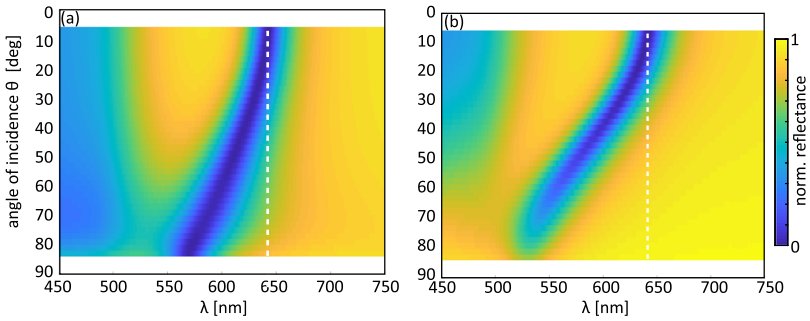

FIG. 3. Measured reflectance from the device under consideration as a function of wavelength λ and angle of incidence for (a) *p*- and (b) *s*-polarization.

$$\tilde{E}_{\mathrm{ref},s}(k_x, k_y) = r_s \tilde{E}_{0s}(k_x, k_y). \tag{1b}$$

Inverse Fourier transforming gives the *p*- and *s*-components of the reflected fields $E_{\mathrm{ref},p}(x, y)$ and $E_{\mathrm{ref},s}(x, y)$ from which the intensity of the output field can be calculated. Here, we assume unpolarized illumination and ignore any polarization effects introduced by the sample. Low spatial frequencies are suppressed in the reflected image and high spatial frequencies are enhanced, on account of the angular response of the screen and the one-to-one correspondence between spatial frequencies k_x, k_y and the wave propagation direction. These enhanced regions correspond to sharp edges in an amplitude object or regions with strong phase gradients in a phase object. Regions dominated by low spatial frequencies, i.e., uniform areas, are absorbed by the filter and appear darker. Figures 2(a) and 2(b) show an amplitude object and the simulated intensity reflected from the screen at $\lambda = 631$ nm. It is evident that edges in the reflected image [Fig. 2(b)] appear bright compared to regions dominated by low spatial frequencies, thus demonstrating the edge enhancement capabilities. The double ringing at the edges results from the nonlinear transfer function of the screen and the fact that evanescent fields are not collected. The appearance of this effect after spatial frequency filtering was also observed in Ref. 29. Furthermore, regions dominated by sufficiently high spatial frequencies are also present in the vicinity of the edges for micrometer sized images which causes additional artifacts in the reflected image, limiting the ability of the filter to resolve edge-enhanced images of high complexity. Figures 2(c) and 2(d) further demonstrate the conversion of phase gradients resulting from propagation of a plane wave through a pure phase object to measurable variations in intensity in the processed image. The input has a total phase excursion of $\Delta\varphi_{\max} = 3\pi$ rad in Fig. 2(c), with the resulting image in Fig. 2(d) exhibiting intensity variations associated with regions of higher phase gradient. These results demonstrate the potential of the filter to suppress low spatial frequencies in the reflected field enabling edge enhancement and conversion of phase gradients into visible intensity variations as required in many biological imaging applications, particularly, visualization of live biological cells.

III. EXPERIMENTS

In Sec. II, we analyzed the filtering response of the Salisbury screen numerically and showed that it behaves as a high-pass spatial filter. In this section, we verify these results experimentally using a Salisbury screen fabricated from a thin layer of gold on silicon dioxide overlaying a thick gold mirror. The screen was fabricated on a [100] p-type silicon wafer. A titanium adhesion layer with a thickness of 3 nm was deposited on the wafer at 0.2 Å/s followed by a 150 nm thick layer of Au deposited at 0.7 Å/s using an IntlVac NanoChrome II e-beam evaporator. A 155 nm thick layer of SiO_2 was grown on the sample using an Oxford Instruments PLASMALAB 100 PECVD system. The sample was then loaded back into the e-beam evaporator and a 31 nm thick Au film deposited on the SiO_2 layer. The reflectance was measured for both *p*- and *s*-polarizations as a function of angle of incidence using a spectrometer [Agilent Cary 7000 UV-Vis-NIR Universal Measuring Spectrometer (UMS)] with the results shown in Fig. 3. The design of the spectrometer limits the minimum and maximum measurable angle of incidence to 6° and 84°, respectively. The measurements show an absorption of 98.5% of the incident intensity around 640 nm at 6° angle of incidence, shifting toward the blue as the angle of incidence increases for both *p*- and *s*-polarizations, in line with the numerical simulations in Fig. 1. The absorption maximum is shifted by approximately 10 nm compared to the numerical result which we attribute to variations in the dielectric function of gold and silicon dioxide in thin films compared to bulk material as well as an uncertainty of ±10% in deposited film thickness for both fabrication methods. This spectral shift is consistent with our numerical predictions for this thickness uncertainty.

To experimentally confirm the image processing capability of the filter, we demonstrate edge enhancement of an amplitude image and visualize phase gradients in an image with negligible amplitude modulation. A real image of the object is projected onto the

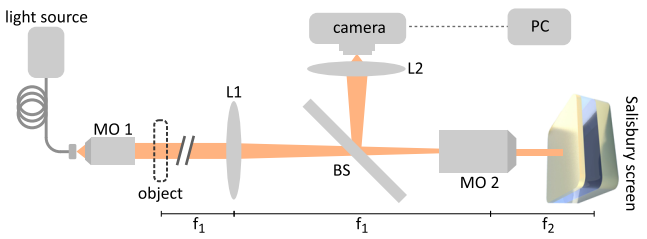

FIG. 4. Köhler-illumination scheme used to demonstrate edge enhancement and phase gradient detection. Spatial frequency mapping is achieved by demagnification with the telescope consisting of L1 and MO2. The distance between the object and L1 is not shown to scale as indicated by the break-sign.

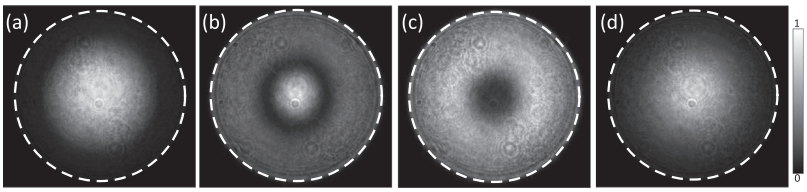

FIG. 5. Measured Fourier plane images in reflectance from the Salisbury screen with central wavelength set to 598 nm (a), 632 nm (b), 640 nm (c), and 694 nm (d) with dashed lines indicating NA = 0.9.

surface of the optical Salisbury screen using the benchtop Köhler-illumination configuration in Fig. 4. Unpolarized light from a supercontinuum laser source (Fianium SC-450-2) is passed through a fiber-coupled tunable filter (Fianium Superchrome VIS-FDS-MM) set to its minimum bandwidth of 5 nm. Light is guided to the setup via a single mode fiber (Thorlabs SM600) and collimated using a NA 0.3 Nikon LU Plan Fluor objective (MO1). The collimated beam is transmitted through the object under investigation which is then projected onto the sample surface via a telescope consisting of a f = 100 mm lens (Thorlabs LA1509-A) (L1), a beam splitter (Thorlabs CM1-BS013), and an infinity corrected NA 0.90 Nikon Plan NCG 100× objective (MO2) with a working distance of 1 mm.

This combination effectively enables 50× demagnification of the image, thus broadening its spatial frequency distribution. The light reflected from the Salisbury filter is imaged onto the camera (L2). As a proof of concept, Fourier plane images were obtained with the object and lens (L1) removed as shown in Fig. 5. These results are consistent with the angular measurements obtained using the spectrometer shown in Fig. 3. The suppression of low spatial frequencies at 640 nm is apparent. It should be noted that the structure behaves as a spatial frequency bandpass filter at shorter wavelengths as apparent from the dark ring in Fig. 5(b). It is, therefore, possible to modify the optical transfer function of the device by changing the wavelength.

To demonstrate edge enhancement, an amplitude image was formed using the figure "2" of a negative USAF-1951 resolution test target (Thorlabs R1DS1N) [Fig. 6(a)]. The results indicate enhanced edges at the absorption wavelength of the Salisbury filter [Fig. 6(c)] not present at shorter [Fig. 6(b)] or longer wavelengths [Fig. 6(d)]. The experimental results are consistent with the numerical findings. It should be noted that the quantitative edge enhancement contrast is sensitive to the spectral bandwidth of the illumination as well as the spatial frequencies generated by the object and those captured by the imaging system. These depend on the sharpness of the edges of the resolution test pattern and the projected image, which are experimentally difficult to quantify. The spectral bandwidth of the illumination implies an effective optical transfer function that is averaged over the bandwidth of the laser system, thereby reducing the contrast between reflected high- and low-spatial frequencies.

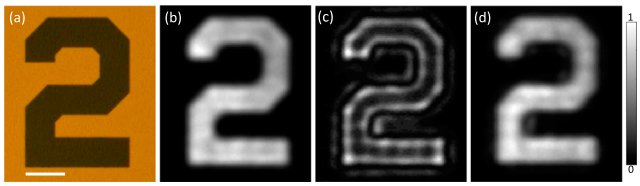

FIG. 6. Demonstration of edge enhancement in amplitude images reflected from the Salisbury screen. (a) Brightfield microscope image in reflection of experimental amplitude object, experimental reflectance from the thin film mirror at (b) 598 nm, (c) 640 nm, and (d) 694 nm. Scale bar is 100 μm.

To confirm the potential for the Salisbury screen to visualize phase gradients, we used a PMMA film with a spatially varying thickness profile in the shape of spherical caps (FINLENS Flyeye 80 LPI) as a test sample with a brightfield microscope image of the sample shown in Fig. 7(a). In order to minimize scattering of light transmitted through the sample, the PMMA film was immersed in index matching oil (Cargille, n_{oil} = 1.518). The brightfield image of the resulting sample is shown in Fig. 7(b) with the thickness modulation becoming almost invisible. The spatial modulation, however, is still apparent in a differential interference contrast (DIC) image of the same sample in Fig. 7(c) indicating a phase modulation resulting from the thickness profile of the PMMA film. Limitations of the phase imaging capability of the absorber arise from its relatively low angular sensitivity resulting in the requirement for demagnification of macroscopic images to elevate the spatial frequency content. This in turn produces ringing artifacts due to spatial frequency components that are not captured by the imaging system and potentially decreased image quality when operating close to the diffraction limit. Figure 7(e) shows images of the PMMA film reflected from the Salisbury screen at the absorption wavelength. While the central part of the spherical caps, associated with low phase gradients, remains dark, the outer parts appear bright indicating a steep phase gradient in line with the DIC image in Fig. 7(c). At shorter [Fig. 7(d)] and longer wavelengths [Fig. 7(f)], the spherical caps appear almost uniform apart from bright lines due to residual scattering at the edges. Horizontal and vertical line profile plots [Figs. 7(g)–7(i)] through the middle of the central spherical cap further highlight the intensity contrast generated by the phase gradient. The line profiles have been averaged over an interval of ±0.56 μm around the horizontal (vertical) center of the lens in order to reduce noise. The results confirm experimentally the ability of the Salisbury filter to convert a phase gradient into a readily measured intensity modulation in the reflected image, in principle permitting phase imaging of biological cells.

As an example, we used a sample of pond-water containing filamentous-algae fixed between two microscope coverslips. In our measurements, the intensity of the incident light was below 30 μW/cm^2, as required to limit the risk of phototoxicity for typical biological samples.[30] The filaments of the algae investigated typically consist of chains of cylindrical cells.[31] The images of the algae reflected from the mirror are shown in Fig. 8 for wavelengths of 598 nm, 638 nm, and 694 nm. While the internal structure of the filaments is not, or only slightly, visible in Figs. 8(a) and 8(c), increased contrast indicating a segmentation of the filament is apparent in

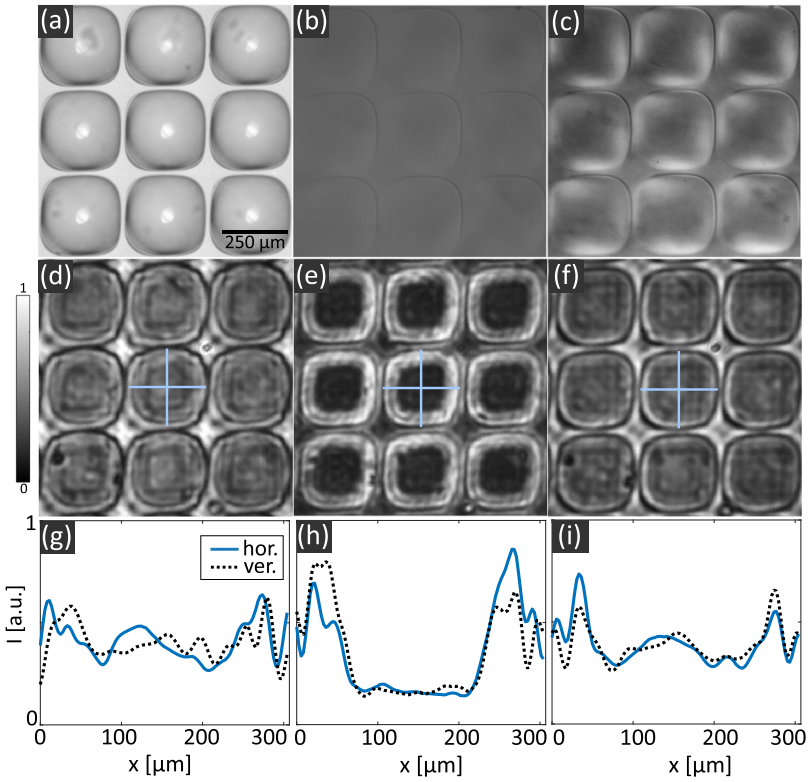

FIG. 7. Experimental demonstration of phase-gradient detection using a PMMA film with spatial thickness modulation as a test object. Brightfield image recorded using white-light illumination of the object without (a) and with (b) index matching oil, differential interference contrast image of lenses immersed in index matching oil (c). Images reflected from the mirror and corresponding line profile plots through the horizontal and vertical center of the central spherical cap (blue crosses) at 598 nm (d) and (g), 640 nm (e) and (h), and 694 nm (f) and (i).

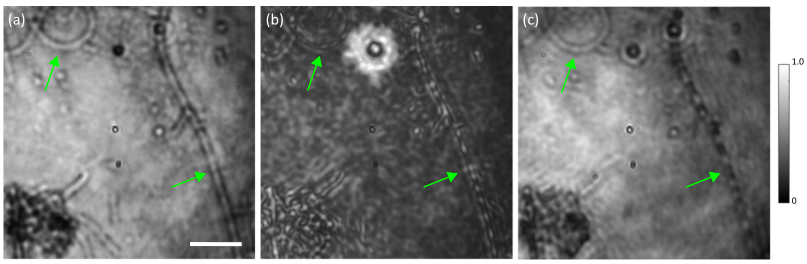

FIG. 8. Demonstration of phase imaging of a biological sample using a filamentous-algae in water indicated by green arrows. Images reflected from the mirror at a wavelength of 598 nm (a), 638 nm (b), and 694 nm (c). Sample scale bar is 250 μm.

Fig. 8(b) at the resonance wavelength of the absorber. Increased contrast in other, unidentified features in the pond water is also apparent. The image quality is limited due to remaining noise from backreflection of the coverslips and scattering by the surrounding water as well as the demagnification of the image. In summary, these results are the first demonstration of biological phase imaging using the thin-film absorber device and underpin the potential of the absorber to serve as a platform for next-generation biological phase imaging applications.

IV. CONCLUSION

In conclusion, we have demonstrated both computationally and experimentally the all-optical, real-time image processing capability of a two layer thin film absorber structure using the example of an Au/SiO_2/Au multilayer Salisbury screen configuration. We have characterized the wavelength-selective angular response of the device in reflection and demonstrated its highpass-spatial frequency filtering potential. Although the current filter design is limited to reflection, the broad concepts presented here are applicable to transmitting devices. We used this filter to demonstrate edge enhancement of an amplitude image reflected from the surface of the device and demonstrated its ability to convert microscopic phase gradients, typically arising from light directed through biological cells, into intensity variations in the reflected image. The potential of the device as a platform for biological phase imaging was demonstrated using the example of a filamentous algae. The structure presented here supports spatial frequency filtering at a wavelength in the visible spectral range tunable by the choice of the geometric parameters, offering the intriguing possibility of being further able to design highly specialized devices for application-dependent integrated optics. More complex layered structures with additional absorption lines could, for example, have potential for the increased operational bandwidth and the

processing of color images. Devices with adjustable mirror spacing using microelectromechanical systems (MEMS)[32] or a dielectric spacer material with a tunable refractive index such as phase change materials[33] furthermore offer the intriguing possibility of a dynamically tunable optical transfer function. Applications of the presented research lie in the field of live-cell imaging and biological and material imaging approaches where the thin-film absorber could provide cheap and ultracompact alternatives to bulky phase imaging approaches.

ACKNOWLEDGMENTS

Research funded by Australian Research Council Discovery Projects (Grant No. DP160100983) and Future Fellowship scheme (Grant No. FT140100514). This work was performed in part at the Melbourne Centre for Nanofabrication (MCN) in the Victorian Node of the Australian National Fabrication Facility (ANFF).

REFERENCES

[1]D. J. Stephens and V. J. Allan, "Light microscopy techniques for live cell imaging," Science **300**, 82–86 (2003).
[2]E. Hjelmås and B. K. Low, "Face detection: A survey," Comput. Vision Image Understanding **83**, 236–274 (2001).
[3]F. Zernike, "Phase contrast, a new method for the microscopic observation of transparent objects," Physica **9**, 686–698 (1942).
[4]D. Murphy and M. Davidson, "Differential interference contrast (DIC) microscopy and modulation contrast microscopy," in *Fundamentals of Light Microscopy and Digital Imaging* (WILEY-LISS, 2001), pp. 153–168.
[5]C. P. Chen and C.-Y. Zhang, "Data-intensive applications, challenges, techniques and technologies: A survey on big data," Inf. Sci. **275**, 314–347 (2014).
[6]D. L. Pham, C. Xu, and J. L. Prince, "Current methods in medical image segmentation," Annu. Rev. Biomed. Eng. **2**, 315–337 (2000).
[7]D. Solli, G. Herink, B. Jalali, and C. Ropers, "Fluctuations and correlations in modulation instability," Nat. Photonics **6**, 463 (2012).
[8]D. R. Solli and B. Jalali, "Analog optical computing," Nat. Photonics **9**, 704 (2015).
[9]A. Silva, F. Monticone, G. Castaldi, V. Galdi, A. Alù, and N. Engheta, "Performing mathematical operations with metamaterials," Science **343**, 160–163 (2014).
[10]S. K. Case, "Fourier processing in the object plane," Opt. Lett. **4**, 286–288 (1979).
[11]A. Roberts, D. E. Gómez, and T. J. Davis, "Optical image processing with metasurface dark modes," J. Opt. Soc. Am. A **35**, 1575–1584 (2018).
[12]Y. Hwang and T. J. Davis, "Optical metasurfaces for subwavelength difference operations," Appl. Phys. Lett. **109**, 181101 (2016).
[13]T. Davis, K. Vernon, and D. Gómez, "A plasmonic 'ac Wheatstone bridge' circuit for high-sensitivity phase measurement and single-molecule detection," J. Appl. Phys. **106**, 043502 (2009).
[14]C. Guo, M. Xiao, M. Minkov, Y. Shi, and S. Fan, "Photonic crystal slab Laplace operator for image differentiation," Optica **5**, 251–256 (2018).
[15]H. Kwon, D. Sounas, A. Cordaro, A. Polman, and A. Alù, "Nonlocal metasurfaces for optical signal processing," Phys. Rev. Lett. **121**, 173004 (2018).
[16]D. A. Bykov, L. L. Doskolovich, A. A. Morozov, V. V. Podlipnov, E. A. Bezus, P. Verma, and V. A. Soifer, "First-order optical spatial differentiator based on a guided-mode resonant grating," Opt. Express **26**, 10997–11006 (2018).
[17]Z. Dong, J. Si, X. Yu, and X. Deng, "Optical spatial differentiator based on subwavelength high-contrast gratings," Appl. Phys. Lett. **112**, 181102 (2018).
[18]Y. Fang and Z. Ruan, "Optical spatial differentiator for a synthetic three-dimensional optical field," Opt. Lett. **43**, 5893–5896 (2018).
[19]Z. Ruan, "Spatial mode control of surface plasmon polariton excitation with gain medium: From spatial differentiator to integrator," Opt. Lett. **40**, 601–604 (2015).
[20]W. Wu, W. Jiang, J. Yang, S. Gong, and Y. Ma, "Multilayered analog optical differentiating device: Performance analysis on structural parameters," Opt. Lett. **42**, 5270 (2017).
[21]N. V. Golovastikov, D. A. Bykov, L. L. Doskolovich, and E. A. Bezus, "Spatial optical integrator based on phase-shifted Bragg gratings," Opt. Commun. **338**, 457–460 (2015).
[22]D. A. Bykov, L. L. Doskolovich, E. A. Bezus, and V. A. Soifer, "Optical computation of the Laplace operator using phase-shifted Bragg grating," Opt. Express **22**, 25084–25092 (2014).
[23]T. Zhu, Y. Lou, Y. Zhou, J. Zhang, J. Huang, Y. Li, H. Luo, S. Wen, S. Zhu, and Q. Gong, "Generalized spatial differentiation from the spin hall effect of light and its application in image processing of edge detection," Phys. Rev. Appl. **11**, 034043 (2019).
[24]T. Zhu, Y. Zhou, Y. Lou, H. Ye, M. Qiu, Z. Ruan, and S. Fan, "Plasmonic computing of spatial differentiation." Nat. Commun. **8**, 15391 (2017).
[25]W. W. Salisbury, "Absorbent body for electromagnetic waves," U.S. patent 2599944A (10 June 1952).
[26]D. N. Breslauer, R. N. Maamari, N. A. Switz, W. A. Lam, and D. A. Fletcher, "Mobile phone based clinical microscopy for global health applications," PLoS One **4**, e6320 (2009).
[27]P. B. Johnson and R. W. Christy, "Optical constants of the noble metals," Phys. Rev. B **6**, 4370–4379 (1972).
[28]I. Malitson, "Interspecimen comparison of the refractive index of fused silica," J. Opt. Soc. Am. A **55**, 1205–1209 (1965).
[29]A. Cordaro, H. Kwon, D. Sounas, A. F. Koenderink, A. Alù, and A. Polman, "High-index dielectric metasurfaces performing mathematical operations," preprint arXiv:1903.08402 (2019).
[30]S. Wäldchen, J. Lehmann, T. Klein, S. Van De Linde, and M. Sauer, "Light-induced cell damage in live-cell super-resolution microscopy," Sci. Rep. **5**, 15348 (2015).
[31]M. Johnson, S. Shivkumar, and L. Berlowitz-Tarrant, "Structure and properties of filamentous green algae," Mater. Sci. Eng.: B **38**, 103–108 (1996).
[32]S. Kim, G. Barbastathis, and H. Tuller, "MEMS for optical functionality," J. Electroceram. **12**, 133–144 (2004).
[33]S. Cueff, D. Li, Y. Zhou, F. J. Wong, J. A. Kurvits, S. Ramanathan, and R. Zia, "Dynamic control of light emission faster than the lifetime limit using VO_2 phase-change," Nat. Commun. **6**, 8636 (2015).